Strong collapse turbulence in a quintic nonlinear Schrödinger equation

Yeojin Chung[1] and Pavel M. Lushnikov[2]
[1]*Department of Mathematics, Southern Methodist University, Dallas, Texas 75275, USA*
[2]*Department of Mathematics and Statistics, University of New Mexico, Albuquerque, New Mexico 87131, USA*
(Received 20 April 2011; published 14 September 2011)

We consider the quintic one-dimensional nonlinear Schrödinger equation with forcing and both linear and nonlinear dissipation. Quintic nonlinearity results in multiple collapse events randomly distributed in space and time, forming forced turbulence. Without dissipation each of these collapses produces finite-time singularity, but dissipative terms prevent actual formation of singularity. In statistical steady state of the developed turbulence, the spatial correlation function has a universal form with the correlation length determined by the modulational instability scale. The amplitude fluctuations at that scale are nearly Gaussian while the large-amplitude tail of the probability density function (PDF) is strongly non-Gaussian with powerlike behavior. The small-amplitude nearly Gaussian fluctuations seed formation of large collapse events. The universal spatiotemporal form of these events together with the PDFs for their maximum amplitudes define the powerlike tail of the PDF for large-amplitude fluctuations, i.e., the intermittency of strong turbulence.

DOI: 10.1103/PhysRevE.84.036602 PACS number(s): 45.20.−d, 47.27.−i, 42.65.Jx, 52.38.Hb

I. INTRODUCTION

The nonlinear Schrödinger equation (NLSE)

$$i\psi_t + \nabla^2\psi + \alpha|\psi|^2\psi + \beta|\psi|^4\psi = 0 \tag{1}$$

describes a wide class of interacting nonlinear waves and Bose-Einstein condensates. Here t is the time, the Laplacian ∇^2 is considered in the general dimension D, and the constants α and β correspond to the cubic and quintic nonlinearities, respectively. Generally, $\alpha|\psi|^2\psi$ gives the leading-order nonlinear interaction. In many nonlinear systems α can vanish, which results in the quintic nonlinear Schrödinger equation (QNLSE)

$$i\psi_t + \nabla^2\psi + \beta|\psi|^4\psi = 0. \tag{2}$$

The QNLSE applies, e.g., in the Bose-Einstein condensate where the s-wave scattering length is set to zero by tuning the Feshbach resonance [1,2]. The QNLSE also occurs for general NLSE-type systems near the transition from supercritical to subcritical bifurcations [3,4], pattern formation (in the context of the quintic Ginzburg-Landau equation if β is a complex constant) [5], and dissipative solitons (e.g., in lasers) [6]. Another possible experimental realization of Eq. (2) is the optical pulse propagation in an optical fiber using a nonlinear compensator of nonlinearity [7].

The standard cubic NLSE [Eq. (1) with $\beta = 0$] is integrable in one dimension (1D) by the inverse scattering transform [8] with global existence of all solutions. In contrast, the QNLSE (2) with positive real β and any $D \geqslant 1$ can develop a finite-time singularity (blowup) such that the amplitude of the solution reaches infinity in a finite time. The blowup is accompanied by dramatic contraction of the spatial extent of the function ψ, which is called wave collapse or simply collapse [9,10]. A sufficient condition for the collapse is $H < 0$, where

$$H = \int \left(|\nabla\psi|^2 - \frac{\beta}{3}|\psi|^6\right)d\mathbf{r} \tag{3}$$

is the Hamiltonian (energy) and Eq. (2) can be rewritten in the Hamiltonian form

$$i\psi_t = \frac{\delta H}{\delta\psi^*}. \tag{4}$$

The case $D = 1$, which we consider below, is critical because any decrease of the power of nonlinearity in (2) (i.e., replacement of $|\psi|^4\psi$ by $|\psi|^{4+\gamma}\psi$, $\gamma < 0$) results in the global existence of solutions [11–13] for any real β.

Collapse of the QNLSE is not physical, and near singularity different physical regularization mechanisms come into play. These can be numerous nonlinear dissipation mechanisms such as inelastic collisions in Bose-Einstein condensates which result in loss of particles from the condensate [1], optical breakdown and formation of plasma in nonlinear optics [14], or numerous nondissipative regularization effects such as nonlinear saturation in laser-plasma interactions [15], and different dispersive effects or nonparaxiality of optical beam (see, e.g., [16]).

In this paper we consider the 1D QNLSE with linear and nonlinear dissipation so that the QNLSE (2) is replaced by the following regularized QNLSE (RQNLSE):

$$i\psi_t + (1 - ia\epsilon)\partial_x^2\psi + (1 + ic\epsilon)|\psi|^4\psi = i\epsilon\phi, \tag{5}$$

which can be also called a complex quintic Ginzburg-Landau equation. Here x is the spatial coordinate replacing the general $\mathbf{r}$, and $0 < \epsilon \ll 1$ is a small parameter so that to leading approximation $\epsilon \to 0$, the QNLSE (2) is valid. The coefficient $a \sim 1$ determines linear dissipation and the coefficient $c \sim 1$ is responsible for nonlinear dissipation. The linear dissipation has a viscositylike form and can result, e.g., from angular-dependent losses or optical filtering [17,18]. The nonlinear dissipation in the RQNLSE corresponds to three-photon absorption in optics [14] or four-body collisions which cause loss of atoms from the Bose-Einstein condensate [19]. The term $i\epsilon\phi$ describes the general forcing in the system. Specific examples of the realization of the RQNLSE (5) are, e.g., propagation of light in a ring cavity with Kerr nonlinearity (see, e.g., [20]) or any quite general propagation of waves

in nonlinear media with complex dispersion and nonlinear dissipation [21].

The right-hand side (RHS) of Eq. (5) provides forcing and depends on the specific physical model. We consider two types of forcing. First is a deterministic forcing

$$\phi = \hat{b}\psi, \tag{6}$$

which corresponds to a linear instability (amplification) in a system. Here $\hat{b}$ is the linear integral operator over x such that its spatial Fourier transform b_k is the multiplication operator $\phi_k = b_k\psi_k$, where b_k determines the k dependence of the amplification. Below, if not mentioned otherwise, we implicitly assume the simplest case of k-independent amplification as $\hat{b}\psi = b\psi$ and thus Eq. (6) takes the form

$$\phi = b\psi, \tag{7}$$

where b is the positive constant.

The second type is a random additive forcing

$$\phi = \xi(t,x), \tag{8}$$

where the stochastic term ξ is a random Gaussian variable, zero on average, which is δ correlated in time and has a finite spatial correlation such that

$$\langle \xi(t_1,x_1)\xi^*(t_2,x_2)\rangle = \delta(t_1 - t_2)\chi(|x_1 - x_2|). \tag{9}$$

Here

$$\chi(|x_1 - x_2|) = b_g \exp[-|x_1 - x_2|/l_c], \tag{10}$$

l_c is the correlation length of the pump, $\langle\cdots\rangle$ denotes averaging over the statistics of ξ, and b_g is the normalization constant.

Forcing results in the pumping of energy into the system described by the RQNLSE and subsequent formation of multiple collapse events randomly distributed in space and time as shown in Fig. 1(a). Figure 1(b) shows a zoom-in into the temporal evolution of the spatial profile of a typical collapse event which involves growth and subsequent decay of the collapse amplitude.

After the initial transient, the solution of the RQNLSE achieves a statistical steady state (i.e., state of the developed turbulence) as shown in Fig. 2 through the time dependence of the integral

$$N = \int |\psi|^2 dx, \tag{11}$$

which has the meaning of either the number of particles in a Bose-Einstein condensate, or the optical power (or sometimes energy) in optics; it is also called the wave action in oceanography and many other nonlinear wave applications [21]. Below we refer to the number of particles as N. After reaching the statistical steady state shown in Fig. 2(a), N remains constant on average for arbitrary large times with small fluctuations around the average value. It is seen in Fig. 2(b) that dissipation is important near large collapses while forcing works all time (because forcing is proportional to N). In the statistical steady state the pumping of particles (forcing) on average is compensated by the dissipation which ensures the state of the developed turbulence.

The focus of this paper is to describe the strong turbulence in the RQNLSE characterized by these nearly singular

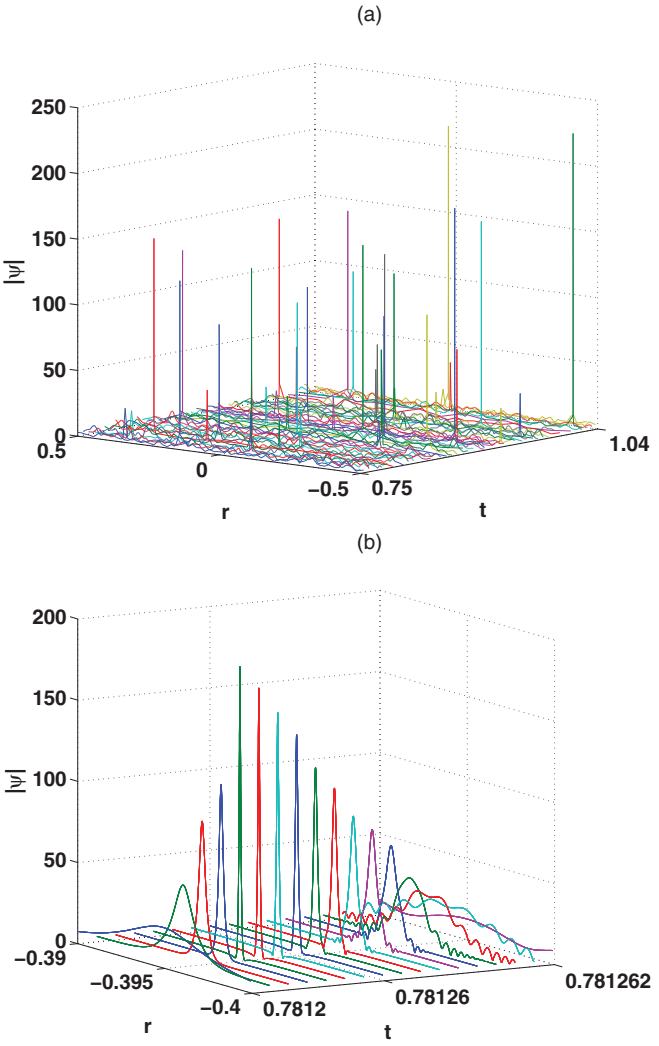

FIG. 1. (Color online) Spatial-temporal form of the solution of the RQNLSE (5) with the deterministic forcing (7), $b = 10^4$, $\epsilon = 2 \times 10^{-3}$, and $a = c = 1$ for different moments of time. (a) Collapses (seen in plot as sharp peaks) occur at random spatial positions and random times. (b) Zoom-in at evolution of single collapse event is shown for a smaller time interval and a smaller spatial extent than in (a). It is seen that the collapse amplitude grows initially, then goes through a maximum, and finally decays due to dissipative effects. Colors are added to (a) and (b) for illustration purposes only to help distinguish different moments of time.

collapse events. By strong turbulence (we also call it strong collapse turbulence) we mean turbulence with strong non-Gaussian fluctuations as opposed to weak turbulence with nearly Gaussian fluctuations [21]. The strong non-Gaussian fluctuations are usually refer to as intermittency of turbulence [22]. The classical example of strong turbulence is Navier-Stokes turbulence. The old problem of the description of strong turbulence in the Navier-Stokes equations through singularities of the Euler equations still remains unsolved [22]. The forced Burgers equation is a very rare example of an analytical description of strong turbulence in which the tail of the probability density function (PDF) for negative gradients follows a well-established $(-7/2)$ power law [23], dominated by the spatiotemporal dynamics near the formation of singular

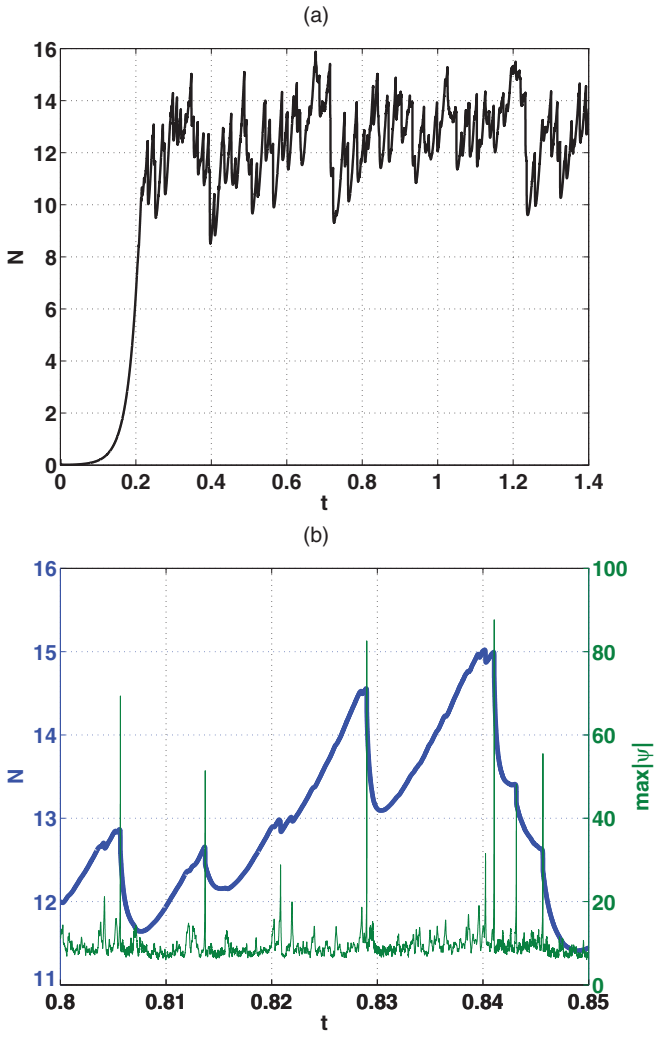

FIG. 2. (Color online) Time dependence of the number of particles N for numerical simulation of the RQNLSE (5) with the deterministic forcing (7) (left axis, thick solid line) superimposed on the time evolution of the maximum value of $|\psi|$ (right axis, solid line). Parameters are $b = 10^4, a = c = 1, \epsilon = 2 \times 10^{-3}$, and the random small-amplitude initial condition is used. (a) Initially N grows until the statistical steady state of developed turbulence is achieved so that N remains constant on average over time. (b) Zoom-in at a smaller scale in t. Solid thick curve [blue (dark gray)] corresponds to $N(t)$. Solid thin curve [green (light gray)] shows time dependence of maximal spatial value of $|\psi|$. Scale for N is on the left vertical axis and scale for max $|\psi|$ is on the right vertical axis. It is seen that sharp decreases of N are due to the dissipation from large collapses. These decreases are compensated on average by growth of N from the linear forcing.

shocks (i.e., by preshocks). The spectrum of the strong optical turbulence was considered for the two-dimensional cubic nonlinear Schrödinger equation in Ref. [24] and the power law tail of the PDFs of the amplitude fluctuations was considered in Refs. [25] and [26]. Strong turbulence in the RQNLSE was first studied in Refs. [27] and [28], with the (-8) PDF power law scaling suggested in Ref. [27]. Here we show that (-8) is only an approximate scaling and it is determined by fluctuations of the background waves which seed collapses as well as by the self-similar form of the collapsing solutions. We also found that the power law of the PDF tail is only weakly sensitive to the type of forcing [linear amplification (7) vs additive random forcing (8)] for $\epsilon \ll 1$, showing a universal turbulence picture.

The paper is organized as follows. In Sec. II we consider the small-amplitude fluctuations of the background of RQNLSE turbulence, show the universality of the spatial and temporal correlation functions, and relate the correlation scale of these fluctuations to the scale of the modulational instability. In Sec. III we review the collapsing self-similar solution of the RQNLSE for $\epsilon = 0$ and establish the universality of the self-similar solution for $\epsilon \neq 0$ as a basic building block for large-amplitude fluctuations. In Sec. IV A we provide the results of numerical calculations of the PDFs for the amplitude fluctuations and for the collapse maxima. In Sec. IV B we derive the analytical expression for the tail of the PDFs for amplitudes and compare with numerics. In Sec. V the main results of the paper and future directions are discussed. In the Appendix we discuss the details of the numerical methods used.

II. MODULATIONAL INSTABILITY AND FLUCTUATIONS OF THE BACKGROUND

The forcing term in the right-hand side of the RQNLSE (5) pumps the number of particles N into the system until the statistical steady state (also called the developed turbulence state) is reached as shown in Fig. 2(a) for a particular example of the deterministic forcing (7). The system in the developed turbulence state does not have a memory of the initial conditions because of the modulational instability. That instability was derived for the cubic NLSE [29] (see also, e.g., [21]) but it is straightforward to generalize it for the RQNLSE as follows. The RQNLSE (5) with $\epsilon = 0$ has a spatially uniform solution $\psi = \psi_0 \exp(i|\psi_0|^4 t)$. Linearization on the background of that solution in the form $\psi = \exp(i|\psi_0|^4 t)[\psi_0 + \delta\psi \exp(\nu t + ikx)]$ with $|\delta\psi/\psi_0| \ll 1$ gives the following instability growth rate ν for the wave number k:

$$\nu^2 = k^2(4|\psi_0|^4 - k^2). \tag{12}$$

The instability occurs for $|k| < 2|\psi_0|^2$ with the unstable branch $\mathrm{Re}[\nu(k)] = \nu(k) > 0$ reaching a maximum of $\nu(k)$ for

$$k_{\max}^2 = 2|\psi_0|^4. \tag{13}$$

For $\epsilon \neq 0$, the expressions (12) and (13) are still approximately valid provided $\nu(k_{\max}) = 2|\psi_0|^4 \gg 1/\tau_f$, where τ_f is the typical time of forcing. For the deterministic forcing (7), $\tau_f = (\epsilon b)^{-1}$, while for the stochastic forcing (8), τ_f can be estimated from the condition that dissipation on average is compensated by the forcing. Then $\tau_f \sim \min[(\epsilon c p_0^4)^{-1}, (\epsilon a k_0^2)^{-1}]$, where p_0 is the typical amplitude of the fluctuation of $|\psi|$ and k_0 is the typical wave vector, which is estimated from (13) as $k_0 \sim k_{\max}$. Recalling now our assumption that $a \sim 1$ and $c \sim 1$, we arrive at a simpler estimate $\tau_f \sim (\epsilon p_0^4)^{-1}$, e.g., using the parameters of Fig. 2 we obtain that $1/\tau_f \simeq 20 \ll \nu(k_{\max}) \simeq 3 \times 10^2$.

Thus the dynamics of the background of turbulence can be characterized by the typical amplitude of the fluctuations p_0 and the spatial scale $1/k_{\max} = 1/(2^{1/2} p_0^2)$. For simulations we define $p_0 = (N/L_0)^{1/2}$, where $L_0 = \int dx$ is the

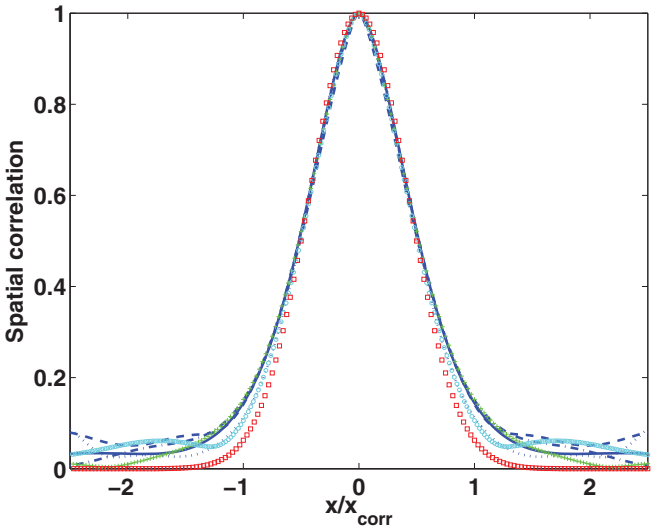

FIG. 3. (Color online) Absolute value of the normalized spatial correlation function $|S(x)/S(0)|$ vs $x/x_{\rm corr}$. Parameters are $\epsilon = 5\times10^{-3}$, $a=c=1$, $b=10^4$ (solid blue line), $\epsilon = 2\times10^{-3}$, $a=c=1$, $b=10^4$ (dash-dotted blue line), $\epsilon=10^{-3}$, $a=c=1$, $b=10^4$ (dashed blue line), $\epsilon=2\times10^{-3}$, $a=c=1$, $b=2\times10^3$ (dotted blue line), $\epsilon=2\times10^{-3}$, $a=1$, $c=2$, $b=10^4$ (green crosses), and $\epsilon=2\times10^{-3}$, $a=2$, $c=1$, $b=10^4$ (light blue circles). Red squares correspond to a Gaussian function $\exp[-4\ln 2(x/x_{\rm corr})^2]$ which has a unit FWHM.

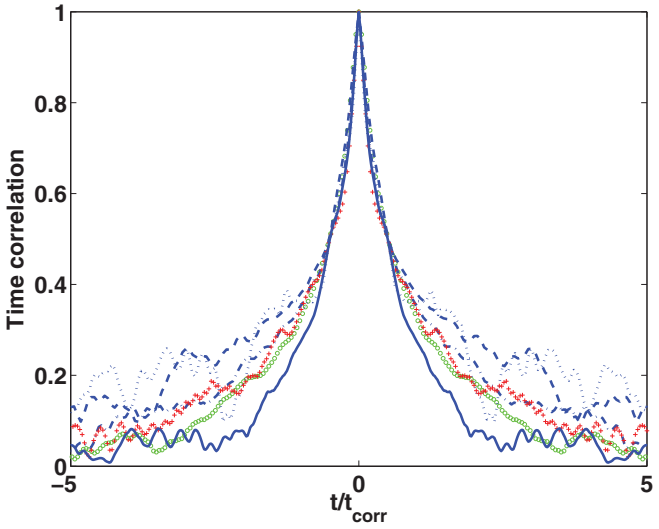

FIG. 4. (Color online) Absolute value of the normalized temporal correlation function $|P(t)/P(0)|$ vs $t/t_{\rm corr}$. Parameters are $\epsilon = 5\times10^{-3}$, $a=c=1$, $b=10^4$ (green circles), $\epsilon=2\times10^{-3}$, $a=c=1$, $b=10^4$ (dash-dotted blue line), $\epsilon=10^{-3}$, $a=c=1$, $b=10^4$ (dashed blue line), $\epsilon=2\times10^{-3}$, $a=c=1$, $b=2\times10^3$ (dotted blue line), $\epsilon=2\times10^{-3}$, $a=1$, $c=2$, $b=10^4$ (red crosses), and $\epsilon=2\times10^{-3}$, $a=2$, $c=1$, $b=10^4$ (solid blue line).

computational domain (without loss of generality we set $L_0 = 1$ in our simulations, as described in Appendix). We determine the correlation length $x_{\rm corrvv}$ of ψ through the full width at half maximum (FWHM) of the spatial correlation function $S(x) = \langle\psi(x_0,t)\psi^*(x_0+x)\rangle$. Here, $\langle\cdots\rangle$ denotes averaging over space and time, which is assumed by ergodicity to give the same result as the average over the ensemble of simulations. Figure 3 shows $|S(x)/S(0)|$ vs $x/x_{\rm corr}$ for a set of simulations with different sets of parameters. Each curve is calculated in the statistical steady state. It is seen that $|S(x)/S(0)|$ is well approximated by the universal function of $x/x_{\rm corr}$ which is close to a Gaussian function $\exp[-(x/x_0)^2]$, while $S(0)=p_0^2$ and x_0 is chosen from the condition to have the same FWHM of the Gaussian function and $|S(x)/S(0)|$. It implies that $x_0/x_{\rm corr} = 1/(2\sqrt{\ln 2})$. Note that with an increase of the ensemble of simulations [i.e., the simulation time used to calculate $S(x)$], the value of $\mathrm{Im}[S(x)]$ approaches 0 and the tails of $\mathrm{Re}[S(x)]$ keep decreasing.

We also determine the correlation time $t_{\rm corr}$ of ψ through the FWHM of the temporal correlation function $P(t) = \langle\psi(x,t_0)\psi^*(x,t_0+t)\rangle$. Figure 4 shows $|P(t)/P(0)|$ as a function of the normalized time $t/t_{\rm corr}$ calculated in the statistical steady state. It is seen that for different sets of parameters, $|P(t)/P(0)|$ is well approximated by a universal function of $t/t_{\rm corr}$. The fluctuations in the tails of $|P(t)/P(0)|$ in Fig. 4 are due to the finite size of the statistical ensemble, and these tails decrease with increase of that ensemble.

Figure 5 shows that the dependence of $p_0(x_{\rm corr})$ is well approximated by

$$p_0^2 x_{\rm corr} = \text{const} \simeq 0.48 \qquad (14)$$

for different values of the parameters of the RQNLSE and for three different types of forcing. This gives another indication that the modulational instability determines the correlation length $x_{\rm corr}$ through the amplitude of the background fluctuations p_0 in agreement with Eq. (13).

Here, the first type is the standard forcing (7) which, while not introducing any scale by itself (it pumps energy into all Fourier modes k), creates the scale $x_{\rm corr}$ indirectly through the development of the modulational instability. Circles in Fig. 5 correspond to that type of forcing.

The second type is a particular example of the general type of forcing (6). We define it by introducing a cutoff wave number $k_{\rm cutoff}$ for the amplification:

$$b_k = b_0 \neq 0,\ |k| \leqslant k_{\rm cutoff};\quad b_k = 0,\ |k| > k_{\rm cutoff}. \qquad (15)$$

In Figs. 5 and 6, for this second type of forcing we use (6) and (15) with $k_{\rm cutoff} = 10\pi$ which means that only 11 modes are amplified. The resulting $N(t)$ dependence in Fig. 6 is similar to that of Fig. 2. In the simulation of Fig. 6, $k_{\rm max} \simeq 2p_0^2 \simeq 20 \sim k_{\rm max}$, and thus $k_{\rm cutoff} \sim k_{\rm max}$. Squares in Fig. 5 correspond to this type of forcing.

The third type is a random additive forcing (8). Figure 7 shows the $N(t)$ dependence from simulations with a random forcing, and the result is similar to Figs. 2 and 6. Again after an initial transient, N reaches the statistical steady state with small fluctuations around the average value. The average value of N remains constant for arbitrarily large times. The diamonds in Fig. 5 correspond to this type of forcing.

We conclude that the turbulence in the RQNLSE is independent of the type of forcing used (up to the normalization). The scale of the forcing itself (if it exists) is not important, and the correlation length is determined by the modulational instability scale. The qualitative picture is the following: the interplay between forcing and dissipation in the RQNLSE defines the

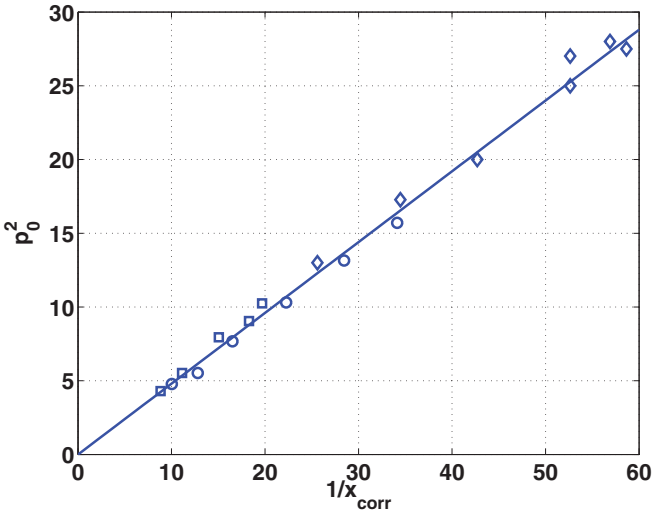

FIG. 5. (Color online) Dependence of p_0^2 on $x_{\rm corr}^{-1}$, where $x_{\rm corr}$ is the FWHM of the spatial correlation function $S(x)$. Circles correspond to the case of k-independent deterministic forcing with $a=1$, $b=10^3$, $c=1$, $\epsilon=2\times10^{-3}$; $a=1$, $b=2\times10^3$, $c=1$, $\epsilon=2\times10^{-3}$; $a=1$, $b=3\times10^3$, $c=1$, $\epsilon=2\times10^{-3}$; $a=2$, $b=10^4$, $c=1$, $\epsilon=2\times10^{-3}$; $a=1$, $b=10^4$, $c=2$, $\epsilon=2\times10^{-3}$; $a=1$, $b=10^4$, $c=1$, $\epsilon=5\times10^{-3}$, from leftmost to rightmost. Squares are for k-limited deterministic forcing (6),(15) with $k_{\rm cutoff}=10\pi$ for $a=1$, $b=10^3$, $c=1$, $\epsilon=2\times10^{-3}$; $a=1$, $b=3\times10^3$, $c=1$, $\epsilon=2\times10^{-3}$; $a=2$, $b=10^4$, $c=1$, $\epsilon=2\times10^{-3}$; $a=1$, $b=10^4$, $c=2$, $\epsilon=2\times10^{-3}$; $a=1$, $b=10^4$, $c=1$, $\epsilon=2\times10^{-3}$, from leftmost to rightmost. Diamonds are for random forcing with $a=1$, $b_g=250$, $c=1$, $\epsilon=5\times10^{-3}$; $a=1$, $b_g=1250$, $c=1$, $\epsilon=5\times10^{-3}$; $a=1$, $b_g=1250$, $c=1$, $\epsilon=2\times10^{-3}$; $a=1$, $b_g=2500$, $c=1$, $\epsilon=2\times10^{-3}$; $a=2$, $b_g=5000$, $c=1$, $\epsilon=2\times10^{-3}$; $a=1$, $b_g=5000$, $c=2$, $\epsilon=2\times10^{-3}$; $a=1$, $b_g=5000$, $c=1$, $\epsilon=2\times10^{-3}$, from leftmost to rightmost. $l_c=0.02$ in all cases. Solid line has a slope 0.48 in accordance with (14).

amplitude p_0 and the correlation length $x_{\rm corr}$ to be related by (14).

We also note that the principal difference between RQNLSE and Navier-Stokes turbulence is the absence for the RQNLSE of a well-defined inertial interval at which both forcing and dissipation are not important. For the RQNLSE dissipation and forcing generally act at all scales. Thus a study of the spectrum of $\langle|\psi_k|^2\rangle$ could give much less information compared with, e.g., weak turbulence [21]. Instead below we focus on the study of the tail of the PDFs for large fluctuations.

III. COLLAPSE AND ITS REGULARIZATION IN THE RQNLSE

Fluctuations of background result in multiple formations of collapses in the RQNLSE as shown in Fig. 1. For $\epsilon=0$, the collapsing solution of the RQNLSE has the following self-similar form:

$$\psi(r,t)=\frac{1}{L^{1/2}}V(\rho,\tau)e^{i\tau+iLL_t\rho^2/4},$$
$$\rho=\frac{r}{L},\quad \tau=\int^t\frac{dt'}{L^2(t')}, \tag{16}$$

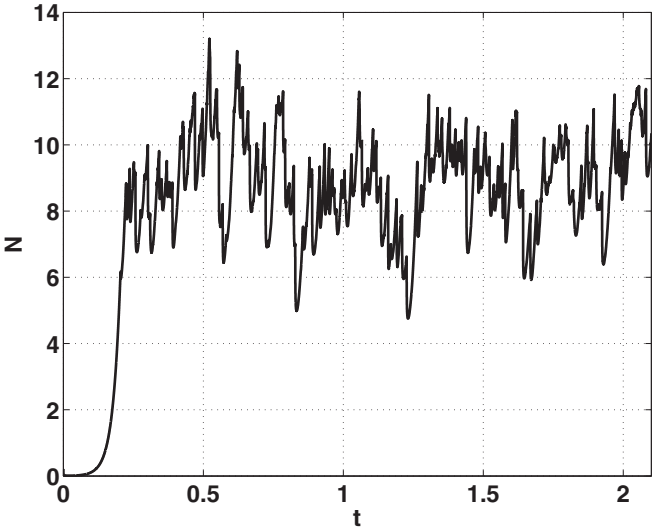

FIG. 6. Time dependence of the number of particles N in the case of k-limited deterministic forcing (6),(15) with $k_{\rm cutoff}=10\pi$. Parameters are $a=c=1$, $b_0=10^4$, $\epsilon=2\times10^{-3}$.

where $L=L(t)$ is the dynamically evolving spatial scale of the collapsing solution at a given moment of time; ρ and τ are sometimes called blow-up variables. $V(\rho,\tau)$ is well approximated for small $L\ll1$ by the ground state soliton solution $R_0(\rho)$: $V(\rho,\tau)\simeq R_0(\rho)$. Here $R_0(x)$ is the positive-definite solution of the equation $-R_0+\partial_x^2R_0+R_0^3=0$, which follows from the RQNLSE assuming that $\psi=e^{it}R_0(x)$ and $\epsilon=0$. The explicit expression for $R_0(x)$ is given by

$$R_0(x)=\frac{3^{1/4}}{(\cosh 2x)^{1/2}}. \tag{17}$$

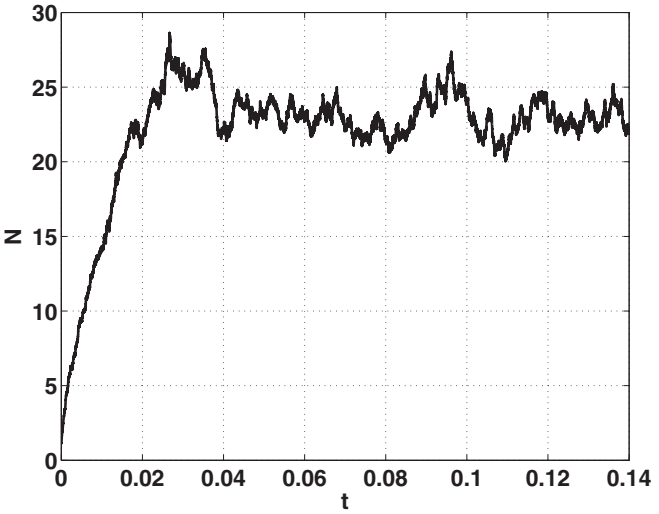

FIG. 7. Time dependence of the number of particles N in the case of random forcing. Parameters are $a=c=1$, $\epsilon=10^{-3}$, $l_c=0.02$, $b_g=12\,500$.

The Hamiltonian (4) [$\beta = 1$ according to (5)] vanishes at the ground state soliton solution (17). The number of particles (11) at (17) is given by

$$N_c = \frac{\sqrt{3}\pi}{2}. \tag{18}$$

N_c determines the boundary between collapsing and noncollapsing solutions: collapse is impossible for $N < N_c$. Note that the ground state soliton solution for the NLSE (1) with $\beta = 0$ in two dimensions (2D) is often referred to as the Townes solution, and it plays a similar role to (17) in the collapse of the 2D NLSE. As $L(t)$ decreases when $t \to t_0$, the spatial distribution of $V(\rho) \to R(\rho)$ for $\rho \lesssim 1$, where t_0 is the collapse time (the time at which a singularity develops in the solution of the RQNLSE with $\epsilon = 0$). It implies that the number of particles in the collapsing region $N_{\text{collapse}} \to N_c$ as $t \to t_0$, i.e., the collapse of the QNLSE is strong as opposed to a weak collapse [13,30] for which the number of particles in the collapsing region vanishes as $t \to t_0$.

The leading-order behavior of $L(t)$ for $t \to t_0$ can be estimated from the scaling analysis as $L(t) \sim (t_0 - t)^{1/2}$ but the criticality of the 1D QNLSE results in the following log-log modification of that scaling [24,31–33]:

$$L \simeq \left(\frac{2\pi(t_0 - t)}{\ln\ln[1/(t_0 - t)]}\right)^{1/2}. \tag{19}$$

The RQNLSE with $\epsilon > 0$ does not allow singular collapses. Instead, for $0 < \epsilon \ll 1$, the collapse amplitude $|\psi|_{\max}(t) \equiv \max_x |\psi(x,t)|$ goes (as a function of time) through a maximum $|\psi|_{\max\max} = \max_t |\psi|_{\max}(t)$ at some $t = t_{\max}$ and decays after that as shown in Fig. 8(a). The spatial form of the collapsing solution is still well approximated by (16) and (17) before and shortly after $t = t_{\max}$, as seen in Figs. 9(a), 9(b), and 9(c). It is seen in Fig. 9(a) that with the growth of $|\psi|_{\max}(t)$ the normalized shape of the solution approaches (17). But with the decay of $|\psi|_{\max}(t)$ for $t > t_{\max}$, the normalized shape of the solution departs from (17) and produces growing oscillating tails as seen in Figs. 9(b) and 9(c). In the vicinity of $t = t_{\max}$ the forcing on the RHS of the RQNLSE (5) can be neglected. The resulting equation can be written in rescaled units $t|\psi|^4_{\max\max}$, $x|\psi|^2_{\max\max}$, and $\psi/|\psi|_{\max\max}$ to have exactly the same form, i.e., the RQNLSE without forcing is invariant with respect to these scaling transformations. As shown in Fig. 8(b) vs Fig. 8(a), $|\psi|_{\max}(t)$ rescaled in these units exhibits a universal behavior: all curves collapse on a single curve in the neighborhood of large collapses. That universality is independent of the complicated structure of optical turbulence. We conclude that up to rescaling all collapse events in the RQNLSE are identical, which is qualitatively similar to the universality of the collapse in the QNLSE. This universality is a characteristic feature of the dissipative terms in RQNLSE (5).

The function

$$\gamma \equiv -L\frac{dL}{dt} \tag{20}$$

changes slowly with t compared to L at $t \lesssim t_{\max}$ except in a very small neighborhood of $t = t_{\max}$ as shown in Fig. 10. The dependence of $\gamma(t)$ is shown in Fig. 10 in the rescaled time unit $(t - t_{\max})|\psi|^4_{\max\max}$, as in Fig. 8(b). We determine $L(t)$ numerically from individual collapse events with $|\psi|_{\max\max} > 30$ using (16) and (17) as $L(t) = 3^{1/2}/|\psi|_{\max}(t)^2$. Thus, the universality of each collapse event is seen for $\gamma(t)$ also.

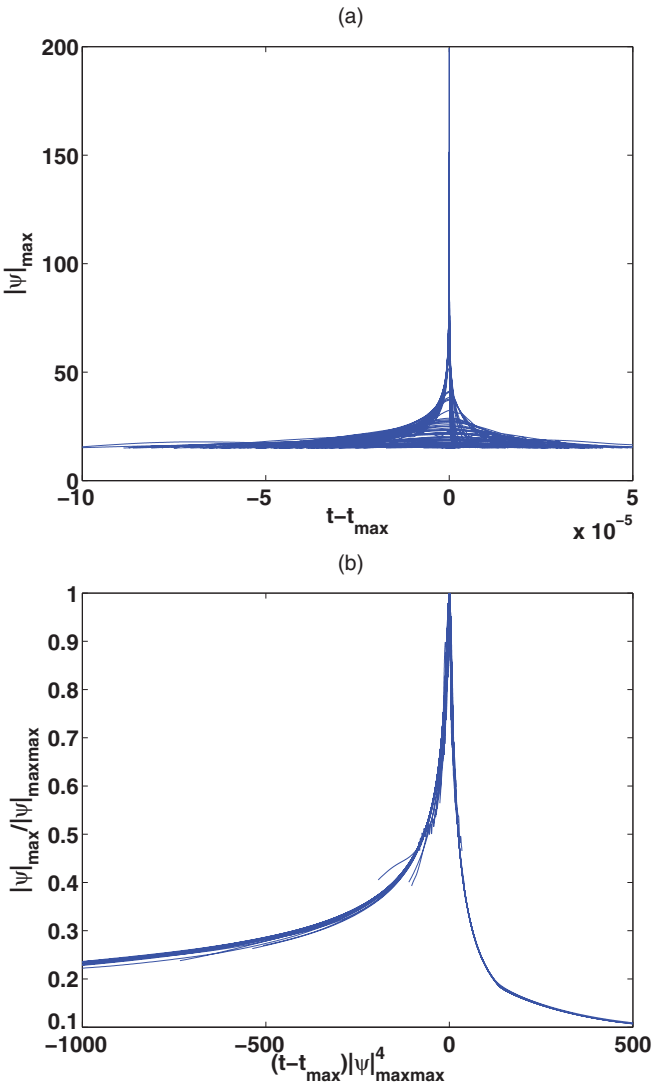

FIG. 8. (Color online) (a) Dependence of $|\psi|_{\max}$ on $(t - t_{\max})$. 75 individual collapse events are collected for $|\psi|_{\max} \geqslant 15$ with parameters $a = 1$, $b = 10^4$, $c = 1$, $\epsilon = 2 \times 10^{-3}$. (b) The same dependence as in (a) but in rescaled units $(t - t_{\max})|\psi|^4_{\max\max}$ and $|\psi|_{\max}/|\psi|_{\max\max}$. The time intervals over which $|\psi|_{\max}/|\psi|_{\max\max}$ are plotted correspond to the time intervals of (a) (i.e., the temporal interval is fixed in nonrescaled units). As a result, collapses with relatively small $|\psi|_{\max\max}$ extend over small intervals of $(t - t_{\max})|\psi|^4_{\max\max}$ in (b).

We conclude in this section that the collapse events in RQNLSE turbulence are all universal ones after a proper rescaling.

IV. PDF OF $|\psi|$

A. PDFs from simulations

Once the amplitude of a collapse event $|\psi|_{\max}$ reaches the maximum $|\psi|_{\max\max}$, it starts decreasing and subsequently the collapse event decays into outgoing waves as seen in Figs. 9(b)

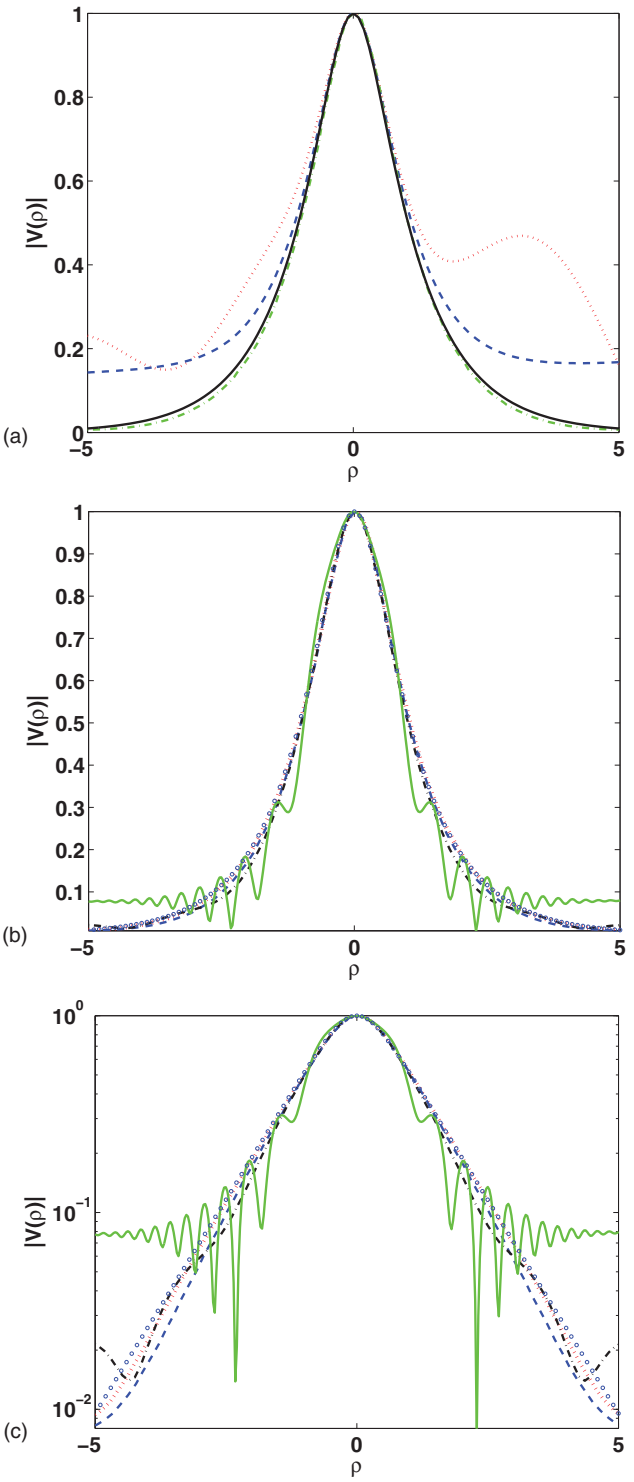

FIG. 9. (Color online) Scaled profiles of numerical solution $|\psi(x)|$ in the vicinity of $t = t_{\max}$ at which $|\psi|_{\max}$ reaches the maximum $|\psi|_{\max\max}$. Parameters are $\epsilon = 2 \times 10^{-3}$, $a = c = 1$, $b = 10^4$. (a) Scaled numerical solution $|\psi(x)|$ at $t = t_{\max} - (4 \times 10^{-5})$ (dotted red), $t = t_{\max} - 10^{-5}$ (dashed blue), and $t = t_{\max}$ (dash-dotted green). Solid black line shows the normalized ground state soliton $\tilde{R}(\rho) = 3^{-1/4} R_0(\rho)$ [Eq. (17)]. (b) Scaled numerical solution $|\psi(x)|$ at $t = t_{\max} - 10^{-8}$ (dotted red), $t = t_{\max}$ (dashed blue), $t = t_{\max} + 10^{-8}$ (dash-dotted black), and $t = t_{\max} + (7 \times 10^{-8})$ (solid green). Circles show the normalized ground state soliton as in (a). (c) Same as (b) on logarithmic scale.

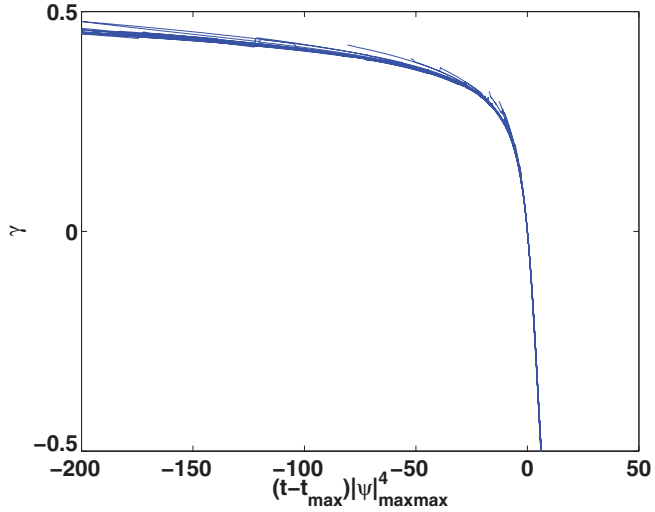

FIG. 10. (Color online) Dependence of $\gamma(t) = -L_t L$ on $(t - t_{\max})|\psi|^4_{\max\max}$. The same individual collapse events as in Fig. 8 are collected for $|\psi|_{\max} \geqslant 30$ in nonrescaled units.

and 9(c). Decaying waves are almost linear, as can be seen from the time dependence of the ratio of the kinetic energy $K = \int |\partial_x \psi|^2 dx$ and the potential energy $P = -\frac{1}{3}\int |\psi|^6 dx$ in Fig. 11(a). Note that the Hamiltonian (3) is the sum of K and P, and during the growth of the amplitude $|\psi|_{\max}$ of the collapse event, these terms nearly cancel each other if the integrals are calculated only inside the collapsing region $\rho \lesssim 1$. In contrast, in the decay phase of the collapse event, the balancing of the terms is strongly violated in favor of K, meaning that the solution is becoming nearly linear. Figure 11(b) shows a zoom-in at a single collapse event. It is seen that while the amplitude of the collapse event decays, the kinetic energy from outgoing waves dominates over the potential energy. Superposition of many of these almost linear waves from multiple collapse events forms a nearly random Gaussian field by the central limit theorem [34]. That random field seeds new collapse events.

Figure 12(a) shows the PDF $\mathcal{P}_r(h_r)$ for the real part of the amplitude ψ to have a value h_r. The PDF for the imaginary part of ψ has the same form. The solid line is a match to the Gaussian distribution [with the same variance as for], which is almost indistinguishable from $\mathcal{P}_r(h_r)$. The PDF $\mathcal{P}_r(h_r)$ is determined from simulations as

$$\mathcal{P}_r(h_r) = \frac{\int \delta\{\mathrm{Re}[\psi(x,t)] - h_r\} dx\, dt}{\int dx\, dt}. \tag{21}$$

Here the integrals are taken over all values of x and all values of t after the turbulence has reached the statistically steady state. We assume ergodicity of the turbulence, i.e., that averaging over space and time is equivalent to averaging over the ensemble of initial conditions (or the stochastic realizations of random forcing for the random forcing case).

In a similar way, $\mathcal{P}(h)$ for the amplitude $|\psi|$ to have a value h is determined from simulations as

$$\mathcal{P}(h) = \frac{\int \delta[|\psi(x,t)| - h] dx\, dt}{\int dx\, dt}, \tag{22}$$

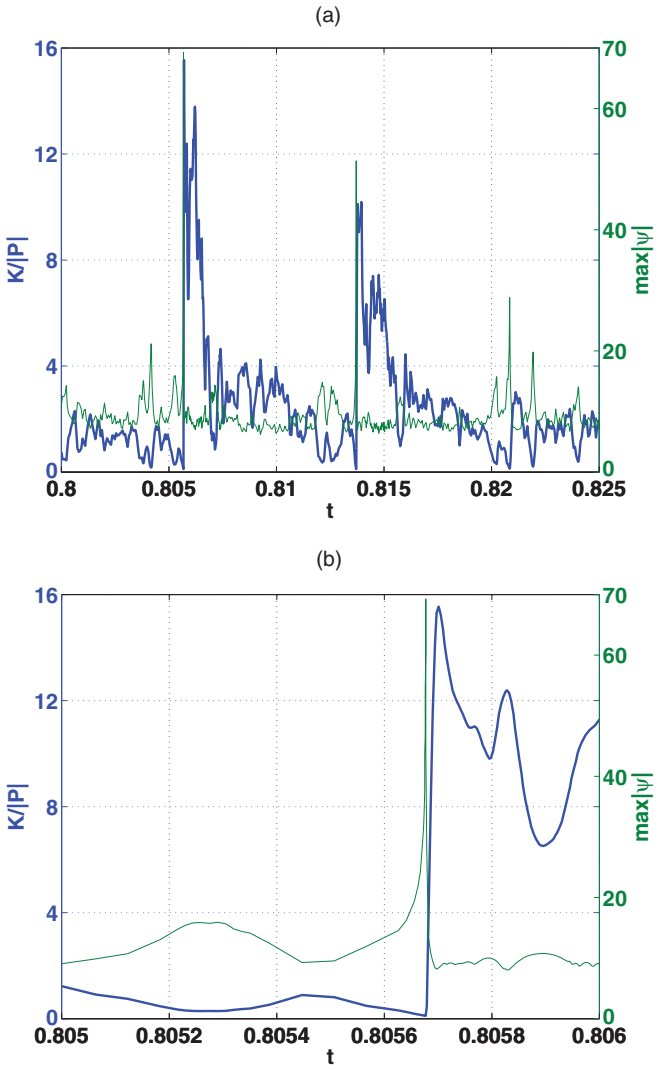

FIG. 11. (Color online) (a) Time dependence of $K/|P|$, where K is the kinetic energy and P is the potential energy defined in the text. Parameters are $a = 1$, $b = 10^4$, $c = 1$, $\epsilon = 2 \times 10^{-3}$. Thick solid curve [blue (dark gray)] corresponds to $K/|P|$. Thin solid curve [green (light gray)] is time dependence of maximal spatial value of $|\psi|$. Scale for $K/|P|$ is on the left vertical axis and scale for max $|\psi|$ is on the right vertical axis. (b) Zoom-in of the same curves as in (a) for a single collapse event.

and, as shown in Fig. 12(b), it is again very close to a Gaussian distribution. Large fluctuations of $|\psi|$ are, however, quite different from the Gaussian distribution and have powerlike tails as shown in Fig. 12(c) on a log-log scale. From comparison of Figs. 12(a), 12(b), and 12(c), we conclude that the fit to the Gaussian distribution works very well for $|\psi| \lesssim 8$; it can be interpreted as the superposition of numerous almost linear waves. For $|\psi| \gtrsim 10$ the PDF has a power-law-like dependence which can be roughly estimated as $\sim h^{-8}$ and which indicates intermittency of the optical turbulence [25].

Figure 13(a) shows the PDF $\mathcal{P}(h)$ for the RQNLSE with the k-limited deterministic forcing (6),(15) and Fig. 13(b) that for the RQNLSE with random forcing (8). It is seen that both of these cases have the same type of pow-

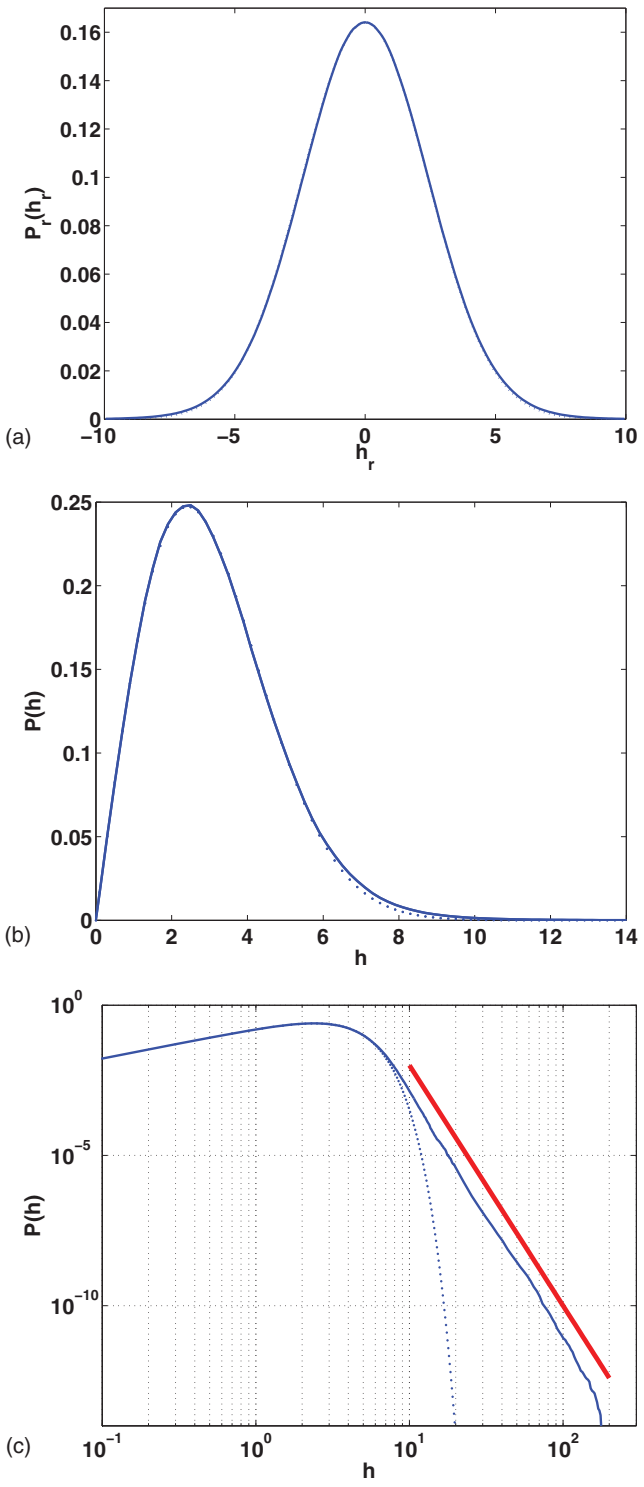

FIG. 12. (Color online) PDFs for simulations with $a = 1$, $c = 1$, $b = 10^4$, $\epsilon = 2 \times 10^{-3}$. (a) PDF $\mathcal{P}_r(h_r)$ for $h_r = \mathrm{Re}(\psi)$. Solid blue line represents numerical result and dotted blue line is for Gaussian distribution $(2\pi)^{-1/2} h_0^{-1} e^{-h^2/(2h_0^2)}$ plotted for comparison. Here the variance $h_0^2 = 5.85$ is obtained from the simulation. (b) PDF $\mathcal{P}(h)$ of $h = |\psi|$ on a linear scale. Solid blue line shows numerical result and dotted blue line is Gaussian distribution $h_0^{-2} h e^{-h^2/(2h_0^2)}$, where h_0^2 is the same variance as in (a). (c) PDF $\mathcal{P}(h)$ of $h = |\psi|$ on a log-log scale. Solid blue line shows numerical result and dotted blue line is the Gaussian distribution as in (b). Thick solid red line shows h^{-8} law for comparison.

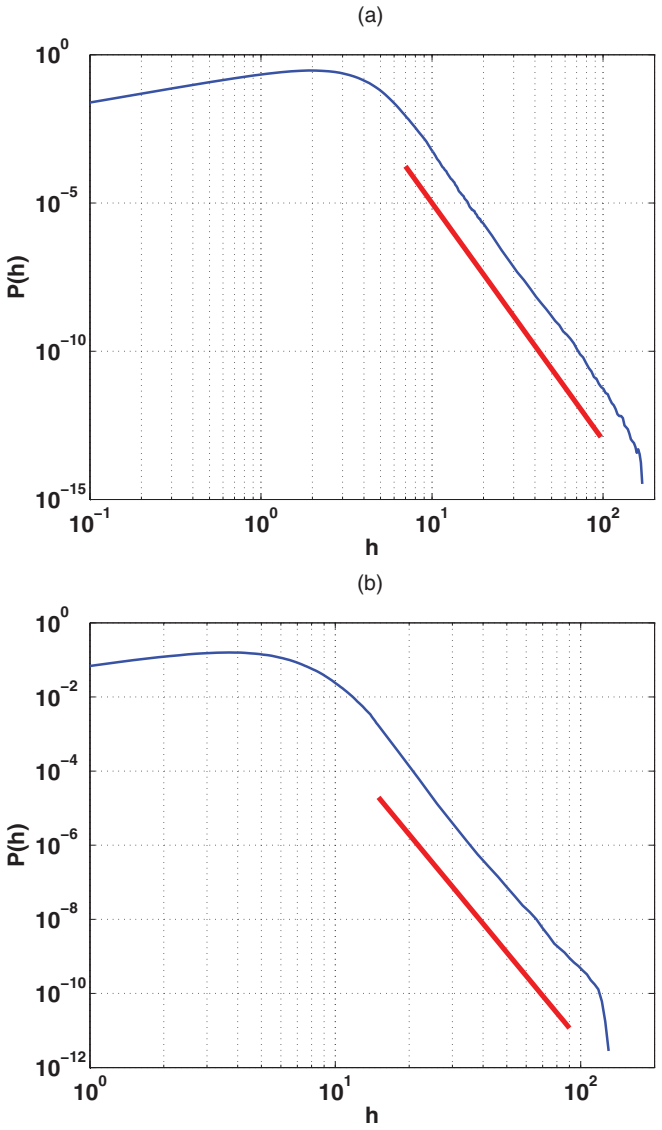

FIG. 13. (Color online) (a) PDF $\mathcal{P}(h)$ of $h = |\psi|$ for k-limited deterministic forcing (6),(15) with $k_{\text{cutoff}} = 10\pi$. Parameters are $a = c = 1, b_0 = 10^4, \epsilon = 2 \times 10^{-3}$. (b) PDF $\mathcal{P}(h)$ of $h = |\psi|$ for random forcing with parameters $a = c = 1, \epsilon = 10^{-3}, l_c = 0.02, b_g = 12\,500$. Solid blue line shows numerical result and thick solid red line shows h^{-8} law for comparison in both figures.

erlike tail as in Figure 12(c). Thus, the powerlike tails are universal for the RQNLSE for $\epsilon \ll 1$ and independent of the type of forcing, indicating universal turbulence behavior.

In order to characterize the relevance of linear and nonlinear dissipation in the PDF $\mathcal{P}(h)$, we consider different parameter values for a and c while fixing ϵ and b. Figure 14(a) shows $\mathcal{P}(h)$ for fixed nonlinear dissipation $c = 1$ and different values of the linear dissipation coefficient a. As a decreases, the slope of the PDF tail becomes steeper, deviating from the h^{-8} power law. For $a < 0.1$, we observe that the shape of the $\mathcal{P}(h)$ tail is very close to the case of $a = 0.1$. Figure 14(b) shows $\mathcal{P}(h)$ for fixed linear dissipation $a = 1$ and variable c. The PDF tail again deviates from the h^{-8} power law as c decreases. The change of tail is more significant at large amplitudes h.

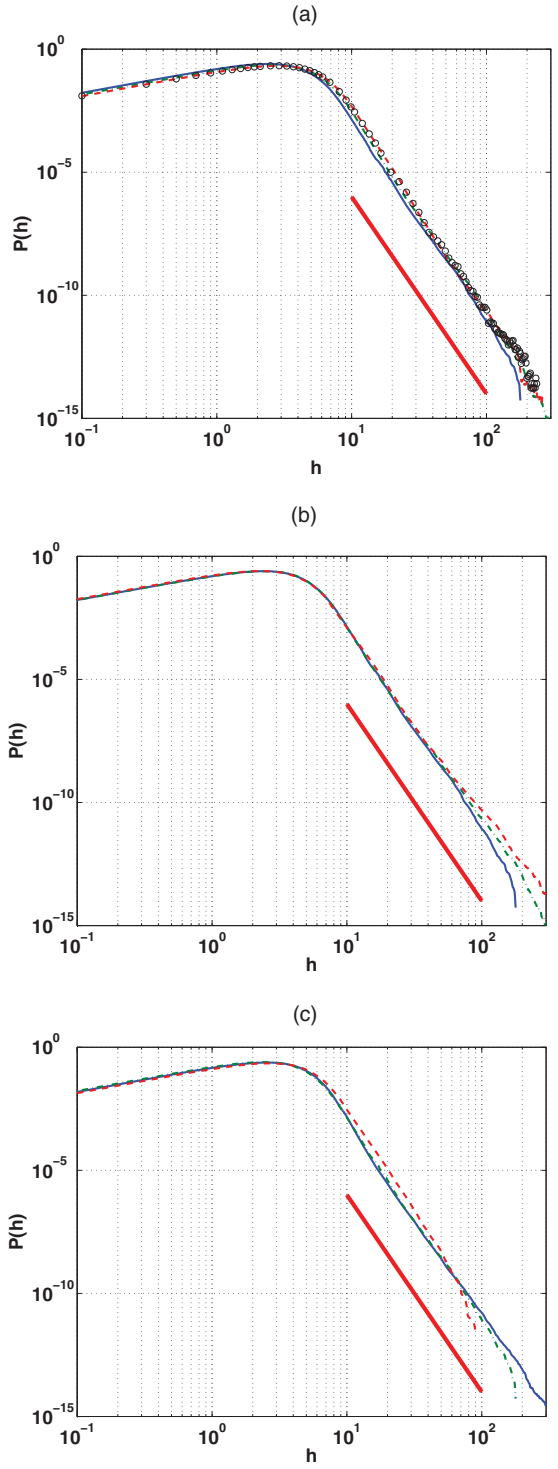

FIG. 14. (Color online) PDF $\mathcal{P}(h)$ of $h = |\psi|$. (a) Parameters are $\epsilon = 2 \times 10^{-3}$, $c = 1$, $b = 10^4$, $a = 0.05$ (black circles), $a = 0.1$ (dashed red), $a = 0.5$ (dash-dotted green), and $a = 1$ (solid blue). Circles are almost indistinguishable from dashed red line and dash-dotted green line. (b) Parameters are $\epsilon = 2 \times 10^{-3}$, $a = 1$, $b = 10^4$, $c = 0.1$ (dashed red), $c = 0.5$ (dash-dotted green), and $c = 1$ (solid blue). (c) Parameters are $a = 1$, $c = 1$, $b = 10^4$, $\epsilon = 10^{-3}$ (solid blue), $\epsilon = 2 \times 10^{-3}$ (dash-dotted green), and $\epsilon = 5 \times 10^{-3}$ (dashed red). Thick solid red line shows h^{-8} power law in all panels.

As c becomes smaller, high-amplitude collapses occur more often, e.g., for $c \sim 0.05$, we frequently observe collapses with

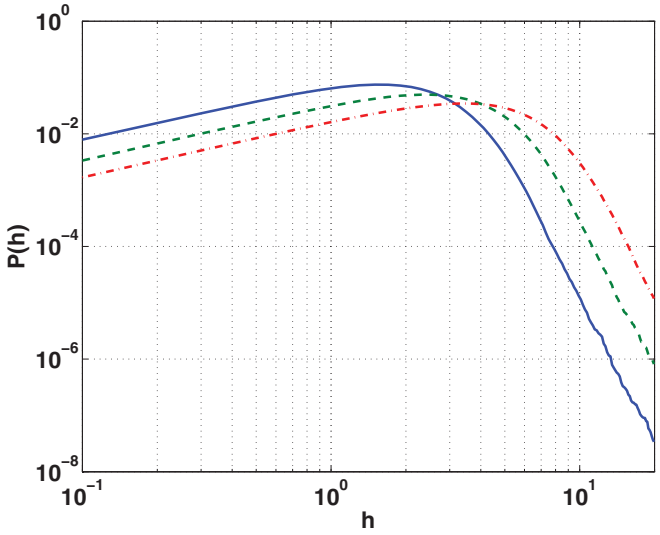

FIG. 15. (Color online) Zoom-in of PDF $\mathcal{P}(h)$ in the range of small $h = |\psi|$. Parameters are $\epsilon = 2 \times 10^{-3}$, $a = c = 1$, $b = 2 \times 10^3$ (solid blue), $b = 10^4$ (dashed green), and $b = 5 \times 10^4$ (dash-dotted red).

amplitude $\gtrsim$500. In contrast, if we change ϵ only, then the tails of $\mathcal{P}(h)$ behave similarly for small $\epsilon \lesssim 3 \times 10^{-3}$ except very large values of h as shown in Fig. 14(c).

We also study the sensitivity of $\mathcal{P}(h)$ to the change of amplification amplitude b. Figure 15 shows that the height of the maximum of $\mathcal{P}(h)$ decreases with increase of b while the position of the maximum $h = h_0$ shifts to the right, indicating increase of the average amplitude $\langle |\psi|^2 \rangle$ (see also Fig. 5). To stress this feature we focus in Fig. 15 on a smaller domain in h and compare with previous figures, while for larger h the tails of $\mathcal{P}(h)$ behave similarly for different b up to the normalization constant.

B. Power-law-like tails of the PDF

We now show that the powerlike tail of $\mathcal{P}(h)$ results from near-singular collapsing events. This approach dates back to the idea of describing strong turbulence in the Navier-Stokes equations through singularities of the Euler equations [22]. Unfortunately, this hydrodynamic problem remains unsolved. The forced Burgers equation remains as the only example of an analytical description of strong turbulence in which the tail of the PDF for negative gradients follows a well-established $(-7/2)$ power law [23], dominated by the dynamics of near-singular shocks. Another example of the analytical description of intermittency is a randomly advected passive scalar; this is an example of turbulent transport described by linear equations [35].

As a first step we calculate the contribution to the PDF from individual collapse events. As shown in Fig. 8, the filament amplitude $|\psi|_{\max}$ rapidly decays after reaching $|\psi|_{\max\max}$ at $t = t_{\max}$. Thus, we neglect the contribution to $\mathcal{P}(h)$ from $t \gtrsim t_{\max}$ in calculating the contribution of the individual filament to $\mathcal{P}(h)$. We define the conditional probability $\mathcal{P}(h|h_{\max})$ for a contribution to the PDF from the collapse event with $|\psi|_{\max\max} \equiv h_{\max}$ and use (16), (17), (20), and (22) as follows:

$$\begin{aligned}\mathcal{P}(h|h_{\max}) &\propto \int^{t_{\max}} dt \int dx \delta\left[h - \frac{1}{L(t)^{1/2}} R_0\left(\frac{x}{L(z)}\right)\right] \\ &\propto \int d\rho \int^{L(t_{\max})} \frac{dL\, L^2}{\gamma} \delta\left(h - \frac{1}{L(t)^{1/2}} R_0(\rho)\right) \\ &\simeq \int \frac{d\rho}{\langle\gamma\rangle h^7} [R_0(\rho)]^6 \Theta\left(\frac{R_0(0)}{L(t_{\max})^{1/2}} - h\right) \\ &= \text{const} \times h^{-7}\, \Theta(h_{\max} - h), \end{aligned} \tag{23}$$

where $h_{\max} = R_0(0)/L(t_{\max})^{1/2} = 3^{1/4}/L(t_{\max})^{1/2}$, and $\Theta(x)$ is the Heaviside step function. Here, we have changed the integration variable from t to L and approximated $\gamma(t)$ under the integral by its average value $\langle\gamma\rangle$ as $\gamma(t) \simeq \langle\gamma\rangle \sim 0.5$. This approximation is valid for $t \lesssim t_{\max}$ outside the neighborhood of $t = t_{\max}$, as seen in Fig. 10.

As a second step we calculate $\mathcal{P}(h)$ by integration over all values of $h_{\max}$ using Eq. (23) as follows:

$$\begin{aligned}\mathcal{P}(h) &= \int dh_{\max} \mathcal{P}(h|h_{\max}) \mathcal{P}_{\max}(h_{\max}) \\ &\simeq \text{const} \times h^{-7} \int dh_{\max} \Theta(h_{\max} - h) \mathcal{P}_{\max}(h_{\max}) \\ &= \text{const} \times h^{-7} H_{\max}(h), \end{aligned} \tag{24}$$

where $\mathcal{P}_{\max}(h_{\max})$ is the PDF for $h_{\max} = |\psi|_{\max\max}$ and $H_{\max}(h) \equiv \int_h^\infty \mathcal{P}_{\max}(h_{\max}) dh_{\max}$ is the cumulative probability for $|\psi|_{\max\max} > h$.

Figures 16(a) and 16(b) show $H_{\max}(h_{\max})$ for different values of parameters. Each curve is calculated after the system reaches the statistical steady state using more than 10^3 collapse events with $h_{\max} > 10$. We verified that an increase of the number of collapse event (i.e., increase of the total simulation time) does not change these curves in any significant way. Figure 16(a) shows that a powerlike dependence $h_{\max}^{-1}$ for $H_{\max}(h_{\max})$, if it exists at all, quickly disappears with increase of ϵ. In Fig. 16(b), $H_{\max}(h_{\max})$ shows that the powerlike dependence $h_{\max}^{-1}$ shifts to larger values $h_{\max}$ with decrease of a. Generally, we see from Figs. 16(a) and 16(b) that for a wide range of parameters, including decrease of ϵ, the dependence of $H_{\max}(h_{\max})$ cannot be approximated as proportional to $(h_{\max})^{-1}$. The assumption that $H_{\max}(h_{\max}) \propto (h_{\max})^{-1}$ comes from (24), and the rough estimate that $\mathcal{P}(h) \propto h^{-8}$ is shown as the thick solid red line of Fig. 12(c). We conclude that this conjecture, first made in [27], appears to be incorrect and h^{-8} is only a very crude approximation for $\mathcal{P}(h)$.

We now verify that Eq. (24) is correct, justifying the assumptions used in (23) and (24). Figures 17(a), 17(b), and 17(c) compare $\mathcal{P}(h)$ from simulations (solid blue lines) with the predictions of Eq. (24) (red circles), where $H_{\max}(h_{\max})$ is obtained numerically and shown in Fig. 16. Also Fig. 16 shows that for $h \gtrsim 20$ Eq. (24) appears to be a much better fit of $\mathcal{P}(h)$ compared with the h^{-8} power law. The normalization constant in Eq. (24) was chosen to fit $\mathcal{P}(h)$ at large h. The deviation of (24) from $\mathcal{P}(h)$ for $h \lesssim 20$ is perhaps due to the decaying of the large-amplitude collapse events into large-amplitude waves [as, e.g., in Fig. 9(c)]. This explanation

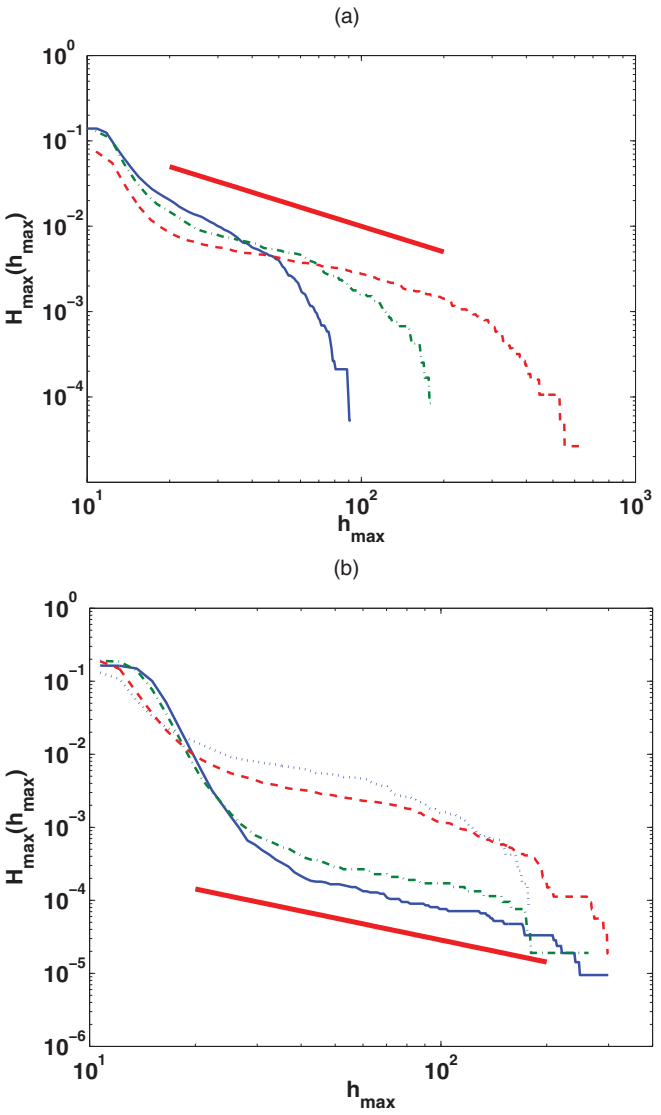

FIG. 16. (Color online) Cumulative probability $H_{\max}(h_{\max})$ for $h_{\max} = |\psi|_{\max}$ and deterministic forcing with $c = 1$, $b = 10^4$. (a) Parameters are $a = 1$, $\epsilon = 5 \times 10^{-3}$ (solid blue), $\epsilon = 2 \times 10^{-3}$ (dash-dotted green), and $\epsilon = 10^{-3}$ (dashed red). (b) Parameters are $\epsilon = 2 \times 10^{-3}$, $a = 0.05$ (solid blue), $a = 0.1$ (dash-dotted green), $a = 0.5$ (dashed red), and $a = 1$ (dotted blue). Thick solid red line shows $h_{\max}^{-1}$ power law for comparison in both panels.

is consistent with the increase of that deviation for smaller values of a as in Fig. 17(c), because the decrease of a causes these large-amplitude, almost linear, waves to exist longer before dissipating, thus giving a bigger contribution to $\mathcal{P}(h)$. We also conclude from Figs. 17(a), 17(b), and 17(c) that, because this deviation is insignificant for $h \gtrsim 20$, the contribution of large-amplitude waves is not important in that range of h. The good agreement between $\mathcal{P}(h)$ and Eq. (24) justifies the assumptions used in derivation of Eq. (24) as well as showing that the intermittency of optical turbulence of the RQNLSE (5) is solely due to collapse dynamics. We also conclude that while the h^{-8} power law appears to be an intermediate fit at best, Eq. (24) works for all values of parameters of the RQNLSE we tested.

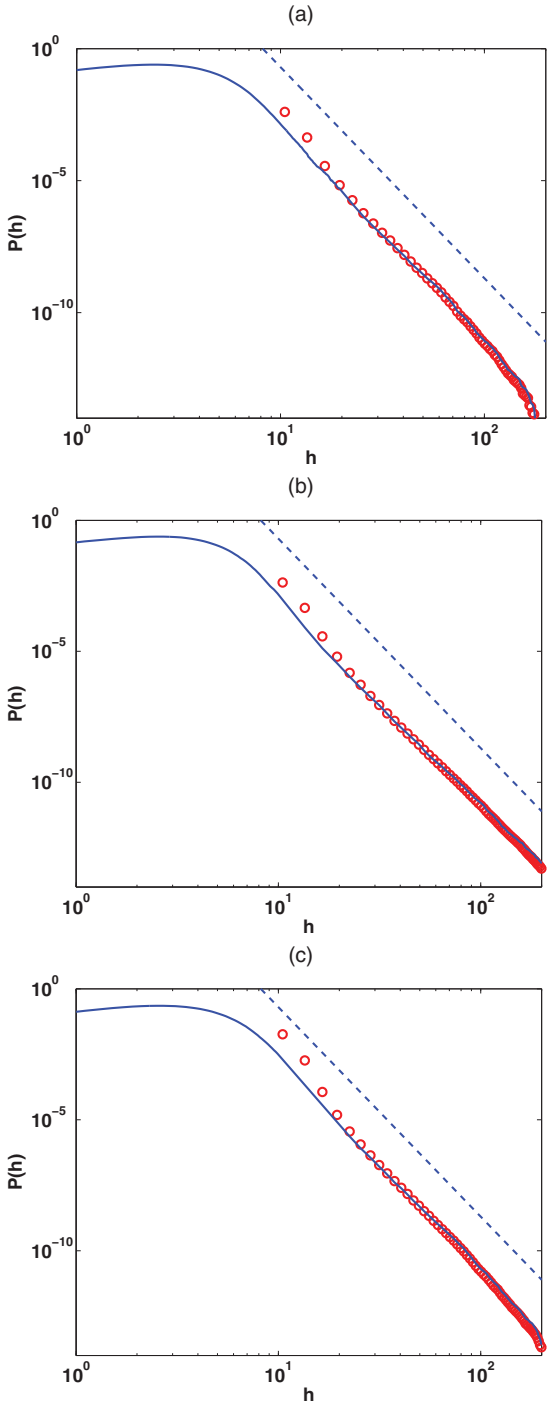

FIG. 17. (Color online) Solid blue curve represents PDF $\mathcal{P}(h)$ for $h = |\psi|$, and dashed blue line shows h^{-8} power law. Red circles correspond to the RHS of Eq. (24). (a) Parameters are $\epsilon = 2 \times 10^{-3}$, $a = c = 1$, $b = 10^4$. (b) Parameters are $\epsilon = 10^{-3}$, $a = c = 1$, $b = 10^4$. (c) Parameters are $\epsilon = 2 \times 10^{-3}$, $a = 0.5$, $c = 1$, $b = 10^4$.

V. CONCLUSION

In this paper we studied strong turbulence in the 1D RQNLSE (5). In the statistical steady state (the state of developed turbulence) a dynamical balance is achieved between forcing which pumps the number of particles N into the system and both linear and nonlinear dissipation. The

RQNLSE has multiple collapse events randomly distributed in space and time. We found that in the state of developed turbulence the spatial and temporal correlation functions have universal forms independent of the particular values of the parameters of the RQNLSE as well as independent of the type of forcing. In particular, we considered deterministic forcing with variable k dependence as well as random forcing. We found that the relation between the correlation length and the average amplitude p_0 has a universal form (14) determined by the modulational instability scale.

The PDF $\mathcal{P}(h)$ of amplitude fluctuations is well approximated by a Gaussian distribution for $h \lesssim 3p_0$. In contrast, $\mathcal{P}(h)$ for $h \gtrsim 4p_0$ has a strongly non-Gaussian tail with powerlike behavior characterizing intermittency of the strong-collapse-dominated turbulence. This tail is determined by Eq. (24), which includes a contribution proportional to h^{-7} from the universal spatiotemporal form of the collapse events as well as a contribution from the cumulative probability $H_{\max}(h)$, the probability of the maximum amplitude of collapse events that exceeds h. We show that $H_{\max}(h)$ is not universal and depends on the parameters of the RQNLSE. For some range of parameters $H_{\max}(h)$ can be roughly estimated as proportional to h^{-1} but it appears to be an intermediate asymptotic at best.

An important problem to be studied in future work is determination of the analytical form of $H_{\max}(h)$ from the parameters of the RQNLSE. This is a challenging problem and will require calculation of the optimal fluctuations of the background which seeds new collapses. Moreover, it will be necessary to find the relation between the size of such optimal fluctuations and the maximum collapse event amplitude $|\psi|_{\max\max}$.

ACKNOWLEDGMENTS

Support of Y.C. was provided by NSF Grant No. DMS 0807131. Work of P.L. was supported by NSF Grant No. DMS 0807131 and DOE Grant No. 1004118.

APPENDIX: NUMERICAL SIMULATIONS OF THE 1D RQNLSE

We provide detailed description of the numerical methods used to produce the simulations described above. We conduct numerical simulation of the RQNLSE (5) by employing a version of the fourth-order split-step method [36] (outlined below) for deterministic forcing as well as the second-order split-step method for random forcing. For efficient computation, we adaptively change the spatial grid size Δx during the time evolution in the spatial domain $-0.5 \leqslant x \leqslant 0.5$. Specifically, if the amplitudes of Fourier components of the solution, $|\psi_k|$, at high frequencies exceed $10^{-10}\max_k|\psi_k|$, we reduce Δx by adding more Fourier modes to the system. If the amplitudes of high-frequency modes are below the criterion, we increase Δx by removing some of the existing Fourier modes. The numerical time step Δt is also updated as Δx changes, following the relation $\Delta t k_{\max}^2 = q_0\pi$. Here $k_{\max} = \pi/\Delta x$ is the maximum wave number determined by the discretization, and we choose the constant factor q_0 small enough to avoid numerical instability. Numerical instability occurs if the change of phase $\Delta\phi = \Delta t k_{\max}^2$ of the highest Fourier harmonics $k_{\max}$ from the linear term of the RQNLSE at one discrete time step Δt is above $\pi/2$: $\Delta\phi \geqslant \pi/2$. In that case a mixing of the Fourier harmonics in the quintic nonlinear term in the RQNLSE can produce artificial (discretization-caused) resonance from the condition $4\Delta\phi = 2\pi$. It implies that to avoid the instability we have to choose $q_0 < 1/2$. In simulations we typically choose $q_0 = 0.2$, which allows us to avoid instability as well as ensuring high accuracy in time stepping. The initial condition of our numerical simulation is a random field with small amplitude whose maximum value is about 1.6.

We write Eq. (5) formally as

$$\psi_t = (\hat{L} + \hat{N})\psi, \tag{A1}$$

where $\hat{L}$ is the linear and $\hat{N}$ is the nonlinear operator, defined by

$$\hat{L}\psi = i(1 - ia\epsilon)\nabla^2\psi + \epsilon\phi, \tag{A2}$$

$$\hat{N}\psi = i(1 + ic\epsilon)|\psi|^4\psi. \tag{A3}$$

Separately both (A2) and (A3) can be solved very efficiently. Here, we approximate the exact solution $\psi(t_0 + \Delta t) = e^{\Delta t(\hat{N}+\hat{L})}\psi(t_0)$ of (A1) over one segment from t_0 to $t_0 + \Delta t$ by the following expression:

$$\psi(t_0 + \Delta t) = e^{c_4\Delta t\hat{N}}e^{d_3\Delta t\hat{L}}e^{c_3\Delta t\hat{N}}e^{d_2\Delta t\hat{L}}e^{c_2\Delta t\hat{N}} \times e^{d_1\Delta t\hat{L}}e^{c_1\Delta t\hat{N}}\psi(t_0), \tag{A4}$$

where

$$c_1 = \frac{1}{2(2-2^{1/3})}, \quad c_2 = \frac{1-2^{1/3}}{2(2-2^{1/3})}, \quad c_3 = c_2, \quad c_4 = c_1, \qquad d_1 = \frac{1}{2-2^{1/3}}, \quad d_2 = \frac{-2^{1/3}}{2-2^{1/3}}, \quad d_3 = d_1. \tag{A5}$$

The split-step expressions (A4),(A5) are fourth-order accurate and are a straightforward generalization of the fourth-order symplectic integration of [36] to non-Hamiltonian systems.

The linear part $e^{\Delta t\hat{L}}$ of the operator splitting can be efficiently calculated by using the fast Fourier transform (FFT) algorithm for the deterministic forcing (6). For the stochastic forcing (8) Eq. (A2) has the form of an inhomogeneous linear differential equation. The homogeneous part of that equation we solve again using FFT while the contribution of the inhomogeneous term is obtained by numerical integration over t for each x. We use the trapezoidal rule for the integration which makes the scheme second order in the random noise case. Therefore, instead of the fourth-order split-step algorithm (A4), we use the standard second-order split-step algorithm $\psi(t_0 + \Delta t) = e^{(1/2)\Delta t\hat{L}}e^{\Delta t\hat{N}}e^{(1/2)\Delta t\hat{L}}\psi(t_0)$ in the random noise case.

The nonlinear part $e^{\Delta t\hat{N}}$ of the operator splitting can be solved exactly as follows. Denote the solution of the nonlinear

part of the RQNLSE as $\psi^{\hat{N}}$. This means that $\psi^{\hat{N}}(t_0+\Delta t) = e^{\Delta t \hat{N}}\psi^{\hat{N}}(t_0)$. According to the RQNLSE, $\psi^{\hat{N}}$ satisfies the following equation:

$$\partial_t \psi^{\hat{N}} = (-c\epsilon + i)|\psi^{\hat{N}}|^4 \psi^{\hat{N}}. \tag{A6}$$

This implies that

$$\frac{d}{dt}|\psi^{\hat{N}}|^2 = -2c\epsilon|\psi^{\hat{N}}|^6, \tag{A7}$$

and hence we find

$$|\psi^{\hat{N}}(t)|^2 = 0 \ \text{ if } \ |\psi^{\hat{N}}(t_0)|^2 = 0, \tag{A8}$$

$$|\psi^{\hat{N}}(t)|^2 = [4c\epsilon(t-t_0) + |\psi^{\hat{N}}(t_0)|^{-4}]^{-1/2} \ \text{ otherwise.} \tag{A9}$$

Using Eqs. (A8) and (A9), we obtain the explicit solution of Eq. (A6),

$$\psi^{\hat{N}}(t_0+\Delta t) = \exp\left[\frac{-c\epsilon + i}{4c\epsilon}\ln[4c\epsilon\,\Delta t|\psi^{\hat{N}}(t_0)|^4 + 1]\right]\psi^{\hat{N}}(t_0). \tag{A10}$$

In the case of random forcing (8), at each time step we independently generate by the Ornstein-Uhlenbeck process [34] the random variable $\xi(x)$, as a function of x with zero mean and correlation length $l_c = 0.02$ that satisfies a stochastic differential equation $\frac{d\xi}{dx} = -l_c^{-1}\xi(x) + \sigma(\Delta t)^{-1/2}\frac{dW(x)}{dx}$, where $\sigma > 0$ and $W(x)$ denotes the Wiener process. This Ornstein-Uhlenbeck process yields an exponential correlation function (9) with $b_g = \sigma^2 l_c/2$. Here the factor $(\Delta t)^{-1/2}$ multiplying dW/dx ensures δ correlation of ξ in time for $\Delta t \to 0$.

[1] L. P. Pitaevskii and S. Stringari, *Bose-Einstein Condensation* (Clarendon, Oxford, 2003).
[2] V. A. Brazhnyi, V. V. Konotop, and L. P. Pitaevskii, Phys. Rev. A **73**, 053601 (2006).
[3] E. A. Kuznetsov, J. Exp. Theor. Phys. **89**, 163 (1999).
[4] D. Agafontsev, F. Dias, and E. A. Kuznetsov, JETP Lett. **87**, 667 (2008).
[5] M. C. Cross and P. C. Hohenberg, Rev. Mod. Phys. **65**, 851 (1993).
[6] J. M. Soto-Crespo, N. Akhmediev, and A. Ankiewicz, Phys. Rev. Lett. **85**, 2937 (2000).
[7] I. R. Gabitov and P. M. Lushnikov, Opt. Lett. **27**, 113 (2002).
[8] V. E. Zakharov and A. B. Shabat, Sov. Phys. JETP **34**, 62 (1972).
[9] S. N. Vlasov, V. A. Petrishchev, and V. I. Talanov, Izv. Vyssh. Uchebn. Zaved., Radiofiz. **14**, 1353 (1971).
[10] V. E. Zakharov, Sov. Phys. JETP **35**, 908 (1972).
[11] J. Ginibre and G. Velo, J. Funct. Anal. **32**, 1 (1979).
[12] M. I. Weinstein, Commun. Math. Phys. **87**, 567 (1983).
[13] C. Sulem and P. L. Sulem, *Nonlinear Schrödinger Equations: Self-Focusing and Wave Collapse* (World Scientific, New York, 1999).
[14] R. W. Boyd, *Nonlinear Optics* (Elsevier, Boston, 2008).
[15] P. M. Lushnikov and H. A. Rose, Phys. Rev. Lett. **92**, 255003 (2004).
[16] G. Fibich and G. Papanicolaou, SIAM J. Appl. Math. **60**, 183 (1999).
[17] W. H. Renninger, A. Chong, and F. W. Wise, Phys. Rev. A **77**, 023814 (2008).
[18] G. Wainblat and B. A. Malomed, Physica D **238**, 1143 (2009).
[19] F. Ferlaino, S. Knoop, M. Berninger, W. Harm, J. P. D'Incao, H.-C. Nägerl, and R. Grimm, Phys. Rev. Lett. **102**, 140401 (2009).
[20] P. M. Lushnikov and M. Saffman, Phys. Rev. E **62**, 5793 (2000).
[21] V. E. Zakharov, V. S. L'vov, and G. Falkovich, *Kolmogorov Spectra of Turbulence* (Springer, New York, 1992).
[22] U. Frisch, *Turbulence: The Legacy of A. N. Kolmogorov* (Cambridge University Press, Cambridge, 1995).
[23] W. E, K. Khanin, A. Mazel, and Y. Sinai, Phys. Rev. Lett. **78**, 1904 (1997).
[24] S. Dyachenko, A. C. Newell, A. Pushkarev, and V. E. Zakharov, Physica D **57**, 96 (1992).
[25] Y. Chung, P. M. Lushnikov, and N. Vladimirova, in *Numerical Analysis and Applied Mathematics*, edited by T. E. Simos, G. Psihoyios, and Ch. Tsitouras, AIP Conf. Proc. No. 1168 (AIP, Melville, NY, 2009), p. 1235.
[26] P. M. Lushnikov and N. Vladimirova, Opt. Lett. **35**, 1965 (2010).
[27] H. Iwasaki and S. Toh, Prog. Theor. Phys. **87**, 1127 (1992).
[28] S. Toh and H. Iwasaki, J. Phys. Soc. Jpn. **61**, 1495 (1992).
[29] V. I. Bespalov and V. I. Talanov, Pis'ma Zh. Eksp. Teor. Fiz. **3**, 471 (1966).
[30] V. E. Zakharov and E. A. Kuznetsov, Sov. Phys. JETP **64**, 773 (1986).
[31] G. M. Fraiman, Sov. Phys. JETP **61**, 228 (1985).
[32] M. J. Landman, G. C. Papanicolaou, C. Sulem, and P. L. Sulem, Phys. Rev. A **38**, 3837 (1988).
[33] B. J. LeMesurier, G. Papanicolaou, C. Sulem, and P. L. Sulem, Physica D **32**, 210 (1988).
[34] C. Gardiner, *Handbook of Stochastic Methods for Physics, Chemistry, and the Natural Sciences* (Springer, New York, 2004).
[35] M. Chertkov, G. Falkovich, I. Kolokolov, and V. Lebedev, Phys. Rev. E **52**, 4924 (1995).
[36] H. Yoshida, Phys. Lett. A **150**, 262 (1990).